IEEE Access
Multidisciplinary : Rapid Review : Open Access Journal

Received May 16, 2019, accepted June 19, 2019, date of publication June 21, 2019, date of current version July 12, 2019.

Digital Object Identifier 10.1109/ACCESS.2019.2924334

Multi-Frequency Holographic Microwave Imaging for Breast Lesion Detection

LULU WANG, (Member, IEEE)
School of Instrument Science and Opto-Electronics Engineering, Hefei University of Technology, Hefei 230009, China
College of Health Science and Environmental Engineering, Shenzhen Technology University, Shenzhen 518118, China

e-mail: lwang381@hotmail.com

This work was supported in part by the National Natural Science Foundation of China under Grant 61701159 and Grant JZ2017GJQN1131, in part by the Natural Science Foundation of Anhui Province under Grant 101413246 and Grant JZ2017AKZR0129, in part by the Fundamental Research Funds for the Central Universities under Grant JZ2018HGTB0236, and in part by the Ministry of Education of the People's Republic of China under Grant 2160311028.

ABSTRACT This paper presents the development of a multi-frequency holographic microwave imaging (HMI) algorithm and investigates the feasibility and effectiveness of the proposed algorithm for breast imaging. A realistic numerical system, including various realistic breast models and image data acquisition model, has been developed using the MATLAB software to demonstrate the working principle of the multi-frequency HMI method. Several numerical experiments have been conducted to evaluate the performance of the proposed method for breast tumor detection. A comparison study of single- and multi-frequency HMIs have been performed to investigate the effectiveness, sensitivity, and accuracy of the proposed method. Results demonstrated that the multi-frequency HMI could improve the breast image quality and accurately detect the small tumors even when they located inside dense tissue. Compared to the single-frequency HMI, the multi-frequency imaging approach could obtain detailed structural information about the breast and identify small lesions more accurately and effectively. The proposed method has the potential to become a great and helpful vision tool for investigating microwave diagnostic techniques.

INDEX TERMS Microwave imaging, holographic microwave imaging, breast cancer, multi-frequency, microwave antenna array.

I. INTRODUCTION

Breast cancer is the common non-skin-related malignancies and the leading cause of cancer-related death among females worldwide [1]. Clinical studies have shown that early diagnosis of breast cancer could improve treatment results and reduce the female cancer-related deaths significantly [2]. X-ray mammography is the gold standard breast imaging tool [3]. However, this technique has some limitations, including ionizing radiation [4], less sensitive for early-stage tumor detection [5], and not suitable for dense breast or women under 40 years of age [6].

Over the past few decades, microwave breast imaging (MBI) has received many interests by researchers worldwide [7]–[10]. Clinical studies on MBI have suggested that microwave imaging (MI) has the potential to become an alternative or additional tool to mammography for diagnosis of breast disease [11]. MBI aims to sense and image the dielectric properties difference between normal and abnormal breast tissues to identify the physiological or pathological conditions of the breast [12]. In terms of safety, MBI approaches do not produce non-ionizing radiation, which is safe for mass imaging or treatment without restrictions. With the fast development of microwave technologies, it is possible to develop cost-effective and portable MBI devices.

The existing MBI methods can be divided into two major categories, which are microwave tomography (MWT) and radar-based microwave imaging. Various MWT algorithms and measurement systems have been developed and investigated for breast cancer detection [13]–[18]. In general, MWT addresses the inverse problem by using iterative algorithms to represent the dielectric properties of tissues. Different from MWT, radar-based MBI uses scattering electric fields from the breast under test to reconstruct images that indicate regions of significant scatterings, such as tumor embedded in healthy tissue. Over the past two decades, several radar-based MBI approaches, including

The associate editor coordinating the review of this manuscript and approving it for publication was Tao Zhou.

confocal microwave imaging [19], tissue sensing adaptive radar [20], microwave imaging via space-time [21] and holographic microwave imaging (HMI) [22], have been proposed and evaluated for investigating breast diseases.

Some limitations of MBI include relatively low resolution, expensive computational cost, unrealistic acquisition apparatus, and incorrect image results in lossy media. The authors recently developed a single frequency HMI for dielectric object detection [23]. Both simulation and experimental results suggested that this approach has the potential for breast imaging. However, the proposed HMI has difficulty in producing a high-quality image, especially when small dielectric inclusions embedded inside the target multi-layer object. It is also challenging to select a more suitable working frequency for the HMI measurement system, which determines the image quality in terms of resolution and penetrability. Moreover, the developed HMI measurement system works at 12.6 GHz, and this working frequency seems a little bit too high for biological tissues.

The image resolution determines the smallest distance between two close inclusions that can be represented in the microwave image. If two inclusions are very close (the distance is below the system resolution), then only one inclusion will appear in the microwave image. The image resolution depends highly on the working frequency range, microwave antenna, and antenna array configuration, as well as imaging algorithm [24]. The resolution is highly related to the shortest wavelength, which is equivalent to the frequency range contained in the illuminating wave through the diffraction limit. The better image resolution would be achieved by using a shorter wavelength. However, a short wavelength also means a smaller penetration depth. Previous studies have suggested that frequency domain imaging may have the potential to solve some problems of BMI approaches [25].

This paper aims to improve microwave image quality by introducing a multi-frequency HMI algorithm and investigates the capabilities of this algorithm for breast lesion detection. A computer system, including various realistic breast phantom and image data collection model, was developed to evaluate the proposed algorithm. The multi-frequency HMI was numerically evaluated on various realistic breast phantoms under practical consideration. Furthermore, the effectiveness and accuracy of the proposed method were studied by comparing the imaging results of single frequency HMI with that of multi-frequency imaging approach.

II. MULTI-FREQUENCY HMI

Figure 1 shows the schematic of the proposed multi-frequency HMI system. The system consists of a microwave source generator, a cylindrical scanner includes an N-element transceiver array (2D plane), and a computer includes a multi-frequency HMI tool. A 3D breast model is placed on the center of the scanner with far-field distance to the transceiver array, and each transceiver simulates as both transmitter and detector. A background medium is assumed in the scanner to ensure microwave signals propagating through the breast and reduce reflection errors.

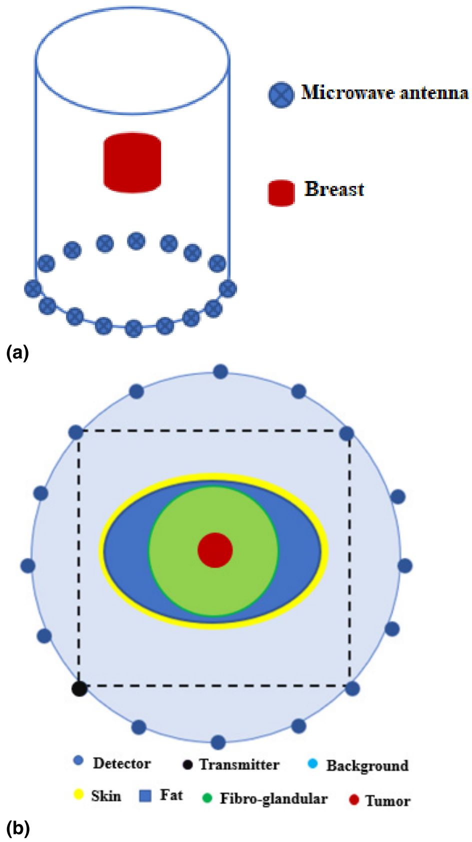

FIGURE 1. (a) Schematic of the multi-frequency HMI system; (b) Microwave antenna array configuration and breast model.

During image data acquisition, the microwave source generator generates microwave signals to the interest region (such as a breast) through each transceiver, and each transceiver records the scattering electric field from the breast. This image data acquisition procedure is repeated for each transceiver to complete a maximum of N × (N − 1) acquisitions. A breast image is reconstructed from the measured scattering signals by using the proposed algorithm. No significant variation occurs in the measurement setup due to high-speed data measurement processing.

A. FORWARD PROBLEM

The total electric field inside the breast is given by:

$$\vec{E}_T^{(p,q)}(\vec{r_T}) = \vec{E}_{inc}^{(p,q)}(\vec{r_T}) + [\varepsilon_b\mu_b\omega^{2(p)} + \nabla\nabla]\int_V \left|\frac{\tilde{\varepsilon}(\vec{s})-\tilde{\varepsilon}_b}{\tilde{\varepsilon}_b}\right| \vec{E}_T^{(p,q)}\left(\vec{r'}\right) \mathrm{G}\left(\vec{r_T},\vec{r'}\right) dV \quad (1)$$

where $\vec{E}_{inc}^{(p,q)}$ being a known incident electric field, $\vec{r_T}$ is the vector position from the target to the transceiver located at $\vec{r_T}$, the angle frequency $\omega^{(p)} = 2\pi f^{(p)}$, $w(p) = 2pif(p) : p = 1, \ldots, P$, $q = 1, \ldots, Q$ at frequency $f^{(p)} = f_{min} + (p - \frac{1}{p} - 1)\Delta f$, f_{min} denotes the minimum frequency, Δf being the frequency range, p being the number of frequencies, and q denotes the number of views. ε_b and μ_b being dielectric permittivity and magnetic permeability of background, respectively. $\tilde{\varepsilon}(\vec{r}) = \varepsilon(\vec{s}) - j\sigma(\vec{s})/\omega^{(p)}$, $\tilde{\varepsilon}_b(\vec{s}) = \varepsilon_b(\vec{s}) - j\sigma_b(\vec{s})/\omega^{(p)}$, ε and ε_b being the relative permittivity of the breast and background, respectively. σ and σ_b being the conductivities of the breast and background, respectively. ∇ is the divergence operator. $\mathrm{G}\left(\vec{r_T}, \vec{r'}\right)$ denotes the Green's function, $\mathrm{G}\left(\vec{r_T}, \vec{r'}\right) = \frac{e^{-j\sqrt{\varepsilon_b\mu_b}\omega^{(p)}\left|\vec{r_T}-\vec{r'}\right|}}{4\pi\left|\vec{r_T}-\vec{r'}\right|}$.

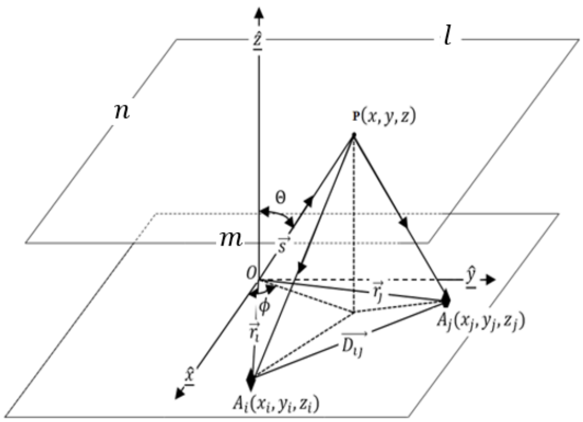

FIGURE 2. Measurement configuration.

B. BACKWORD PROBLEM

As shown in Figure 2, each transceiver measures the scattering electric field from any target point located inside the breast as:

$$\vec{E}_s^{(p,q)}(\vec{r_R}) = \frac{\varepsilon_b\mu_b\omega^{2(p)}}{4\pi}\int_V \left|\frac{\tilde{\varepsilon}(\vec{s}) - \tilde{\varepsilon}_b}{\tilde{\varepsilon}_b}\right| \vec{E}_T^{(p,q)}(\vec{s})\,\mathrm{G}(\vec{r_R}, \vec{s})\,dV \tag{2}$$

where $\vec{r_R}$ is the vector position from the target to the transceiver located at $\vec{r_R}$, $\vec{s}$ denotes the position vector.

The scattering field can be represented as [26]:

$$\begin{aligned}\vec{E}_s^{(p,q)}(\vec{r_R}) &= \frac{\varepsilon_b\mu_b\omega^{2(p)}}{4\pi}\int_V \left|\frac{\tilde{\varepsilon}(\vec{s}) - \tilde{\varepsilon}_b}{\tilde{\varepsilon}_b}\right| \\ &\quad \times \left[a\vec{E}_T^{(p,q)}(\vec{s}) + \left(b\vec{E}_T^{(p,q)}(\vec{s})\cdot\underline{\hat{r_R}}\right)\underline{\hat{r_R}}\right]\mathrm{G}(\vec{r_R})\,dV\end{aligned} \tag{3}$$

where $a = 1 - \frac{j}{\sqrt{\varepsilon_b\mu_b}\omega^{(p)}R} - \frac{1}{\varepsilon_b\mu_b\omega^{2(p)}R^2}$, $b = -1 + \frac{3j}{\sqrt{\varepsilon_b\mu_b}\omega^{(p)}R} + \frac{3}{\varepsilon_b\mu_b\omega^{2(p)}R^2}$, R is the distance between the source and the target point. In this study, $a \approx 1$ and $b \approx -1$. Therefore, the scattering field can be simplified as:

$$\begin{aligned}\vec{E}_s^{(p,q)}(\vec{r_R}) &\cong \frac{\varepsilon_b\mu_b\omega^{2(p)}}{4\pi}\int_V \left|\frac{\tilde{\varepsilon}(\vec{s}) - \tilde{\varepsilon}_b}{\tilde{\varepsilon}_b}\right| \\ &\quad \times [\vec{E}_T^{(p,q)} + (\vec{E}_T^{(p,q)}\cdot\underline{\hat{r_R}})\underline{\hat{r_R}}]\mathrm{G}(\vec{r_R}, \vec{r_T})\,dV\end{aligned} \tag{4}$$

C. IMAGE PROCESSING

As shown in Figure 2, the cross-correlation of the scattering electric field from the target interest region can be measured by any two transceivers located at A_i and A_j as [27]:

$$\vec{V}_{vi}^{(p,q)}(\vec{r_i}, \vec{r_j}) = <\vec{E}_s^{(p,q)}(\vec{r_i})\cdot\vec{E}_s^{*(p,q)}(\vec{r_j})> \tag{5}$$

where <> means time average, $\vec{E}_s^{*(p,q)}$ being the conjugate complex of scattering field. We name this measurement as visibility data. For the N-element array, the total visibility data is $\vec{V}_{vi}^{(p,q)} = \sum_i^N \vec{V}_{vi}^{(p,q)}(\vec{r_i}, \vec{r_j})$, $i \neq j$, $N \geq 3$.

Let us define breast density [28].

$$I^{(p,q)}(\vec{s}) = \left(\frac{\varepsilon_b\mu_b\omega^{2(p)}}{4\pi}\right)^2 \left|\frac{\tilde{\varepsilon}(\vec{s}) - \tilde{\varepsilon}_b}{\tilde{\varepsilon}_b}\right|^2 \vec{E}_T^{(p,q)}(\vec{s})\cdot\vec{E}_T^{*(p,q)}(\vec{s}) \tag{6}$$

The following equation is applied to compute the visibility data.

$$\begin{aligned}\vec{V}_{vi}^{(p,q)}(\vec{r_i}, \vec{r_j}) &= \left(\frac{\varepsilon_b\mu_b\omega^{2(p)}}{4\pi}\right)^2 \iiint_V \left|\frac{\tilde{\varepsilon}(\vec{s}) - \tilde{\varepsilon}_b}{\tilde{\varepsilon}_b}\right|^2 \vec{E}_T^{(p,q)}(\vec{s}) \\ &\quad \cdot\vec{E}_T^{*(p,q)}(\vec{s})\frac{e^{-j\sqrt{\varepsilon_b\mu_b}\omega^{(p)}|\vec{r_i}-\vec{r_j}|\cdot\underline{\hat{s}}}}{s^2}dV\end{aligned} \tag{7}$$

Combining (6) and (7), the visibility formula becomes:

$$\vec{V}_{vi}^{(p,q)}\left(\vec{D_{ij}}\right) = \iiint_V I^{(p,q)}(\vec{s})\frac{e^{-j2\pi\vec{D_{ij}}\cdot\underline{\hat{s}}}}{s^2}dV \tag{8}$$

where $\vec{D_{ij}} = (\vec{r_j} - \vec{r_i})/\lambda_b$, λ_b is background wavelength, $\underline{\hat{s}} = sin\theta cos\phi\underline{\hat{x}} + sin\theta sin\phi\underline{\hat{y}} + cos\theta\underline{\hat{z}}$, $dV = s^2 sin\theta d\theta d\phi ds$. Let us change cartesian coordinates to spherical coordinates, and define variables $l = sin\theta cos\phi$, $m = sin\theta sin\phi$, $n = cos\theta = \sqrt{1 - l^2 - m^2}$. Then, dV can be represented as:

$$dV = s^2 dldmds/n \tag{9}$$

The visibility function is represented as:

$$\vec{V}_{vi}^{(p,q)}\left(\vec{D_{ij}}\right) = \iiint_V I^{(p,q)}(\vec{s})\frac{e^{-j2\pi\vec{D_{ij}}\cdot\underline{\hat{s}}}}{n}dldmds \tag{10}$$

All transceivers located on the same flat array plane, then the visibility function becomes:

$$\begin{aligned}&\vec{V}_{vi}^{(p,q)}\left(u_{ij}, v_{ij}, w_{ij} = 0\right) \\ &\quad = \int_l\int_m\int_n \frac{I^{(p,q)}(s, l, m)}{\sqrt{1 - l^2 - m^2}}e^{-j2\pi(u_{ij}l + v_{ij}m)}dldmds\end{aligned} \tag{11}$$

where $u_{ij} = (\vec{x_j} - \vec{x_i})/\lambda_b$, $v_{ij} = (\vec{y_j} - \vec{y_i})/\lambda_b$, $w_{ij} = (\vec{z_j} - \vec{z_i})/\lambda_b$.

Define the line integral as:

$$\tilde{I}^{(p,q)}(l, m) = \int_s \frac{I^{(p,q)}(s, l, m)}{\sqrt{1 - l^2 - m^2}}ds \tag{12}$$

The visibility data can be compressed as:

$$\vec{V}_{vi}^{(p,q)}\left(u_{ij}, v_{ij}\right) = \iint \tilde{I}^{(p,q)}\left(l, m\right) e^{-j2\pi(u_{ij}l+v_{ij}m)} dldm \quad (13)$$

The following formula is applied to produce the 2D view of the 3D breast:

$$I^{(p,q)} = \iint \vec{V}_{vi}\left(u_{ij}, v_{ij}\right) e^{j2\pi(u_{ij}l+v_{ij}m)} dudv \quad (14)$$

D. METRIC

The peak signal-to-noise ratio (PSNR) measures image quality [29].

$$PSNR = 10log_{10}(peakval^2/\sqrt{MSE}) \quad (15)$$

where *peakval* denotes either specified by the user or taken from the range of the image (such as, it is 255 for uint8 image), mean squared error $MSE = \frac{1}{n}\sum_{i=1}^{n}(Y_i - \hat{Y}_i)^2$, Y denotes the vector observed values of the variable being predicted, and $\hat{Y}$ being a vector of n predictions generated from a sample of n data points on all variables. MSE closer to zero demonstrates better performance.

III. NUMERICAL EXPERIMENTS

This section is devoted to the assessment of the proposed algorithm for breast imaging. For this purpose, a computer system was developed to demonstrate the working principle of the multifrequency HMI algorithm for breast imaging. The computer system consisted of various realistic breast models, a 16-element transceiver array (2D plane) which mounted on the cylindrical scanner (100mm in radius, 100mm in height), and an imaging tool. The breast model was placed in the center of the scanner, and the distance between the breast and the transceiver array was $3.5\lambda_b$ (far-field). According to previous studies [30], the frequency range of 1GHz to 4GHz was selected as the working frequencies.

All numerical evaluations were performed using MATLAB 2018a software on a Dell Precision 5820 workstation which has an Intel Xeon W-2145 CPU with a frequency of 3.7GHz and 256GB of memory.

A. FORWARD SOLVER

A small waveguide antenna was simulated as both transmitter and detector. The electric field illuminated from such transmitter is [31]:

$$\vec{E}_{inc}^{(p,q)}\left(\vec{r_T}, \theta, \phi\right) = \frac{-j\sqrt{\varepsilon_b\mu_b}\omega^{(p)}}{2\pi^2} \times \vec{E}_o^{(p,q)} \frac{\mathrm{e}^{-\mathrm{j}\sqrt{\varepsilon_b\mu_b}\omega^{(p)}\vec{r_T}}}{\vec{r_T}} ABh^{(p,q)}(\theta,\phi)\vec{P}^{(p,q)}(\theta,\phi) \quad (16)$$

where $\vec{E}_o^{(p,q)}$ denotes the amplitude of TE_{10} model, A denotes the board aperture of the antenna, B denotes the narrow aperture of the antenna, $h^{(p,q)}(\theta,\phi)$ and $\vec{P}^{(p,q)}(\theta,\phi)$ denote the radiation pattern and the vector polarization, respectively.

TABLE 1. Breast models.

Model	Structures	Relative Permittivity	σ (S/m)
1	Background	1	0
	Skin	37.952	1.4876
	Fat	5.137	0.14067
	Fibro-glandular	24.4	0.397
2	Background	1	0
	Skin	37.952	1.4876
	Fat	5.137	0.14067
	Fibro-glandular1	24.4	0.397
	Fibro-glandular2	35.55	0.738
	Tumor	58.181	2.5878
3	Background	12	0.4
&	Skin	37.952	1.4876
7	Fat	5.137	0.14067
	Fibro-glandular1	24.4	0.397
	Fibro-glandular2	35.55	0.738
	Tumor	58.181	2.5878
4	Background	12	0.4
	Muscle	33.24	0.866
	Skin	23.83	0.831
	Fat1	1.104	0.005
	Fat2	1.592	0.05
	Fat3	3.545	0.08
	Fibro-glandular1	24.4	0.397
	Fibro-glandular2	35.55	0.738
	Fibro-glandular3	40.49	0.824
5	Background	12	0
&	Muscle	33.24	0.866
6	Skin	23.83	0.831
	Fat1	1.104	0.005
	Fat2	1.592	0.05
	Fat3	3.545	0.08
	Fibro-glandular1	24.4	0.397
	Fibro-glandular2	35.55	0.738
	Fibro-glandular3	40.49	0.824
	Tumor	58.181	2.5878

B. BACKWARD SOLVER

The Born approximation was applied to solve the forward problem [32]. The scattering field was assumed negligible in front of the incident field inside the breast, $\vec{E}_s^{(p,q)} \ll \vec{E}_{inc}^{(p,q)}$, thus, $\vec{E}_T^{(p,q)} \approx \vec{E}_{inc}^{(p,q)}$. The scattering field can be expressed:

$$\vec{E}_s^{(p,q)}(\vec{r_R}) = \frac{\varepsilon_b\mu_b\omega^{2(p)}}{4\pi}\int_V \left|\frac{\tilde{\varepsilon}\left(\vec{s}\right)-\tilde{\varepsilon}_b}{\tilde{\varepsilon}_b}\right| \vec{E}_{inc}^{(p,q)} \frac{\mathrm{e}^{-\mathrm{j}\sqrt{\varepsilon_b\mu_b}\omega^{(p)}\vec{r_R}}}{\vec{r_R}} dV \quad (17)$$

where $\vec{r_R}$ denotes the distance between the target and the transceiver located at $\vec{r_R}$.

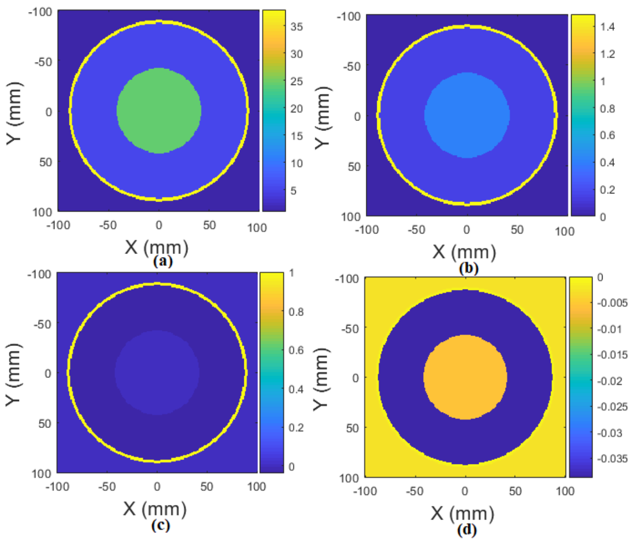

FIGURE 3. Original image of breast model 1: (a) real part (relative permittivity), (b) imaginary part (conductivity); Reconstructed image of breast model 1: (c) real part, (d) imaginary part.

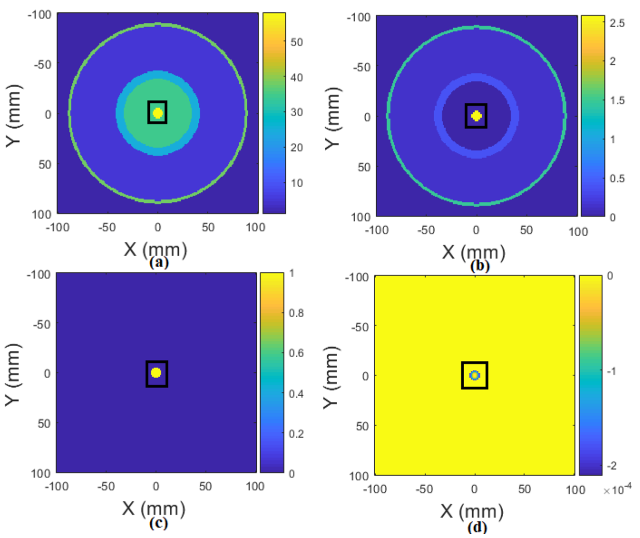

FIGURE 4. Original image of breast 2: (a) real part, (b) imaginary part; Reconstructed image of breast 2: (c) real part, (d) imaginary part.

C. BREAST MODELS

Seven 3D breasts (see Table 1) include noise-free and noise models were developed to evaluate the proposed method for breast imaging. One simplified (breast 1) and three multi-layer breast models (breast models 2, 3, and 7) were developed based on Gaussian function and published dielectric properties of tissues [33]. Three MRI-derived breast models (breasts 4 $\sim$ 6) were developed using MRI images from the Wisconsin University repository (heterogeneously dense breast, ID: 062204) [34]. The noise breast models (breasts 6 and 7) including 10% white Gaussian noise, which were developed based on models 3 and 4. Each model was discretized into 0.5 mm^3 voxels. A sphere-shaped inclusion was developed and positioned inside the breast to simulate tumor.

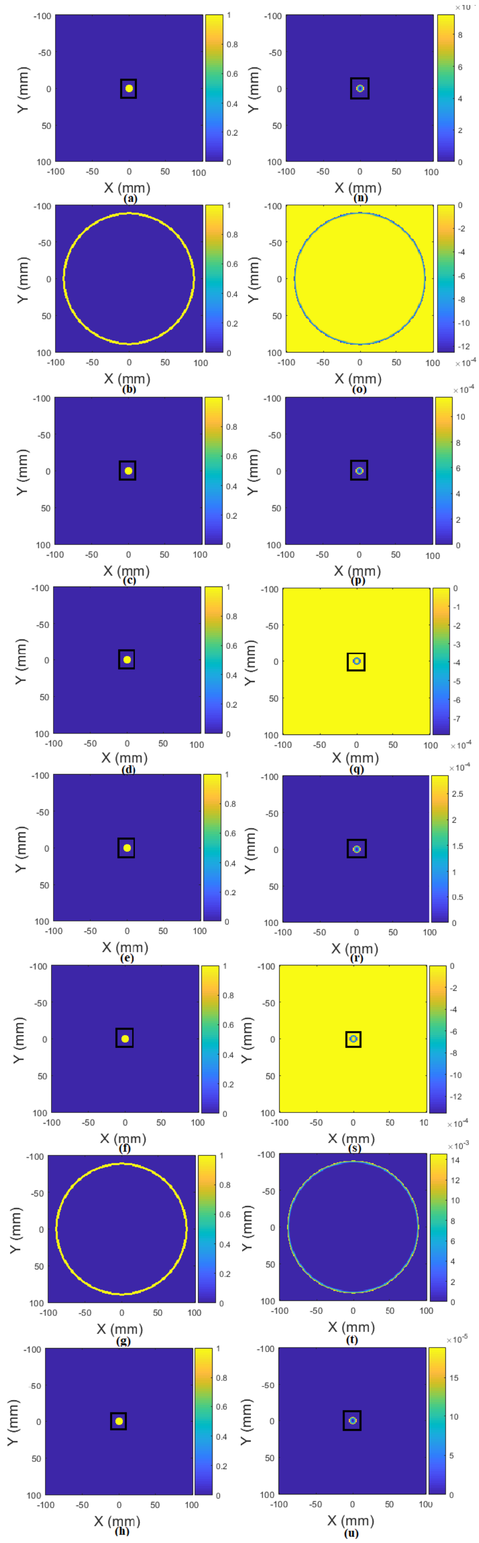

FIGURE 5. Real part of reconstructed image of breast 2: (a) $\varepsilon_r = 5, \sigma = 0$, (b) $\varepsilon_r = 6, \sigma = 0$, (c) $\varepsilon_r = 7, \sigma = 0$, (d) $\varepsilon_r = 8, \sigma = 0$, (e) $\varepsilon_r = 9, \sigma = 0$, (f) $\varepsilon_r = 10, \sigma = 0$, (g) $\varepsilon_r = 11, \sigma = 0$, (h) $\varepsilon_r = 12, \sigma = 0$, (i) $\varepsilon_r = 12$, $\sigma = 0.1$, (j) $\varepsilon_r = 12, \sigma = 0.2$, (k) $\varepsilon_r = 12, \sigma = 0.3$, (l) $\varepsilon_r = 12, \sigma = 0.4$, (m) $\varepsilon_r = 12, \sigma = 0.5$; Imaginary part of reconstructed image of breast 2: (n) $\varepsilon_r = 5, \sigma = 0$, (o) $\varepsilon_r = 6, \sigma = 0$, (p) $\varepsilon_r = 7, \sigma = 0$, (q) $\varepsilon_r = 8, \sigma = 0$, (r) $\varepsilon_r = 9, \sigma = 0$, (s) $\varepsilon_r = 10, \sigma = 0$, (t) $\varepsilon_r = 11, \sigma = 0$, (u) $\varepsilon_r = 12, \sigma = 0$, (v) $\varepsilon_r = 12, \sigma = 0.1$, (w) $\varepsilon_r = 12, \sigma = 0.2$, (x) $\varepsilon_r = 12, \sigma = 0.3$, (y) $\varepsilon_r = 12$, $\sigma = 0.4$, (z) $\varepsilon_r = 12, \sigma = 0.5$.

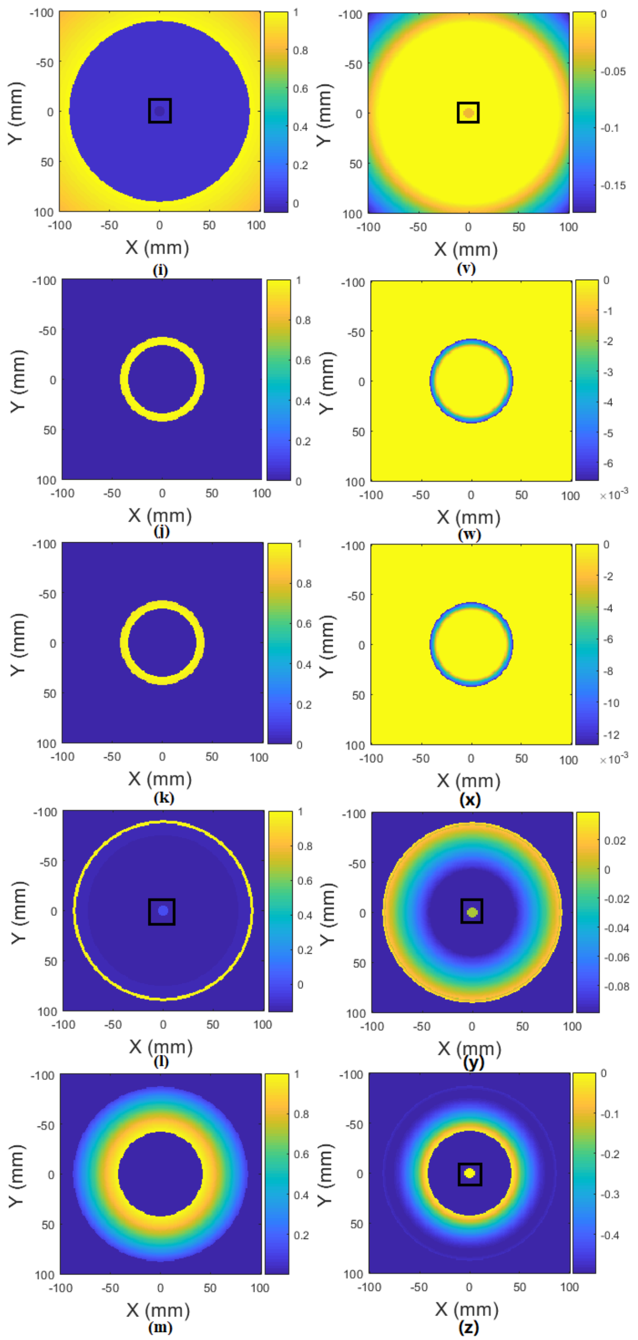

FIGURE 5. ***(Continued.)*** **Real part of reconstructed image of breast 2: (a) $\varepsilon_r = 5, \sigma = 0$, (b) $\varepsilon_r = 6, \sigma = 0$, (c) $\varepsilon_r = 7, \sigma = 0$, (d) $\varepsilon_r = 8, \sigma = 0$, (e) $\varepsilon_r = 9, \sigma = 0$, (f) $\varepsilon_r = 10, \sigma = 0$, (g) $\varepsilon_r = 11, \sigma = 0$, (h) $\varepsilon_r = 12, \sigma = 0$, (i) $\varepsilon_r = 12, \sigma = 0.1$, (j) $\varepsilon_r = 12, \sigma = 0.2$, (k) $\varepsilon_r = 12, \sigma = 0.3$, (l) $\varepsilon_r = 12, \sigma = 0.4$, (m) $\varepsilon_r = 12, \sigma = 0.5$; Imaginary part of reconstructed image of breast 2: (n) $\varepsilon_r = 5, \sigma = 0$, (o) $\varepsilon_r = 6, \sigma = 0$, (p) $\varepsilon_r = 7, \sigma = 0$, (q) $\varepsilon_r = 8, \sigma = 0$, (r) $\varepsilon_r = 9, \sigma = 0$, (s) $\varepsilon_r = 10, \sigma = 0$, (t) $\varepsilon_r = 11, \sigma = 0$, (u) $\varepsilon_r = 12, \sigma = 0$, (v) $\varepsilon_r = 12, \sigma = 0.1$, (w) $\varepsilon_r = 12, \sigma = 0.2$, (x) $\varepsilon_r = 12, \sigma = 0.3$, (y) $\varepsilon_r = 12, \sigma = 0.4$, (z) $\varepsilon_r = 12, \sigma = 0.5$.**

IV. RESULTS

Several simulations were performed to evaluate the possibility of the proposed multi-frequency HMI method for breast lesion detection.

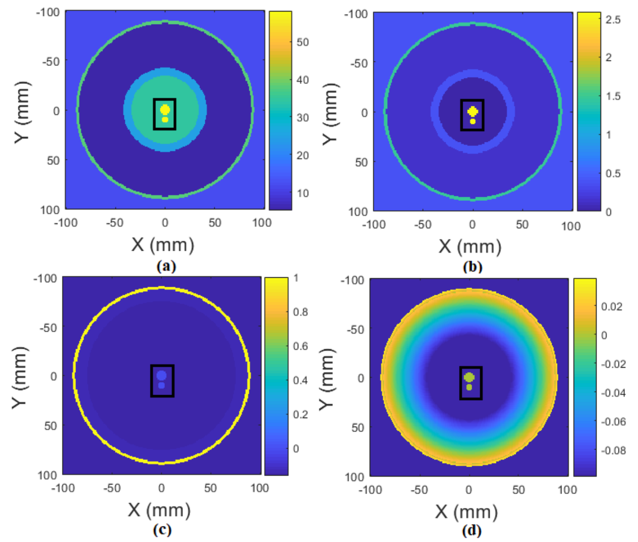

FIGURE 6. Original image of breast 3: (a) real part, (b) imaginary part; Reconstructed image of breast 3: (c) real part, (d) imaginary part.

A. BREAST WITHOUT TUMOR

We first evaluate the performance of the multi-frequency HMI on the simplified breast model 1 ($90 \times 90 \times 50$ mm^3). Air ($\varepsilon_r = 1, \sigma = 0$ S/m) was assumed in the space between the breast and the antenna array plane as well as antennas. Figures 3(a) and 3(b) show the 2D view of the real part (relative permittivity) and imaginary part (conductivity) of the 3D breast 1. Figures 3(c) and 3(d) display the real and imaginary parts of the reconstructed images of the target breast over the frequency range of 1 GHz and 4GHz, respectively. All internal structures of the breast under test could be fully observed in both real and imaginary parts of the reconstructed images.

B. MULTI-LAYER BREAST PHANTOMS

Figures 4(a)-4(b) present the real part (relative permittivity) and imaginary part (conductivity) of breast 2 ($100 \times 100 \times 50$ mm^3), including a 3-mm-thick skin layer, fat, fibro-glandular 1 (42 mm in radius), fibro-glandular 2 (34 mm in radius) and one tumor (5mm in radius, squared in black) located at (0 mm, 0 mm, 0 mm). The breast and transceivers all immersed in air ($\varepsilon_r = 1$, $\sigma = 0$ S/m). The real and imaginary parts of the multi-frequency imaging results over the $1 \sim 4$ GHz band are displayed in Figure 4(c) and Figure 4(d), respectively. Results demonstrated that only tumor could be observed in the reconstructed image. However, other internal structures of the breast include skin, fat, and two fibro-glandular tissues could not be represented in the image.

We also investigated the performance of the proposed method by using different types of mediums. Figure 5 shows the multi-frequency imaging results when breast model 2 and transceivers immersed in different mediums. The results demonstrated that the internal structures of the breast and tumor could be represented in the reconstructed image

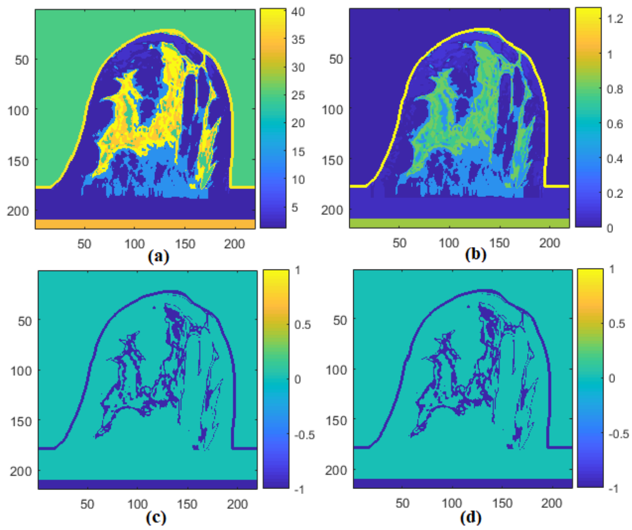

FIGURE 7. Original image of breast 4: (a) real part, (b) imaginary part; Reconstructed image of breast 4: (c) real part, (d) imaginary part.

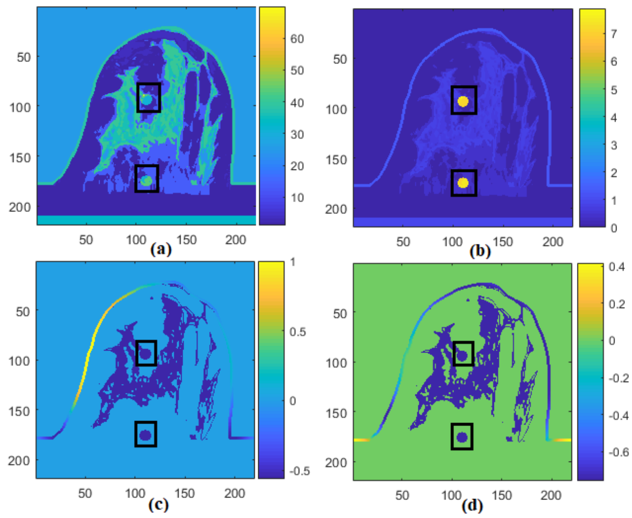

FIGURE 8. Original image of breast 5: (a) real part, (b) imaginary part; Reconstructed image of breast 5: (c) real part, (d) imaginary part.

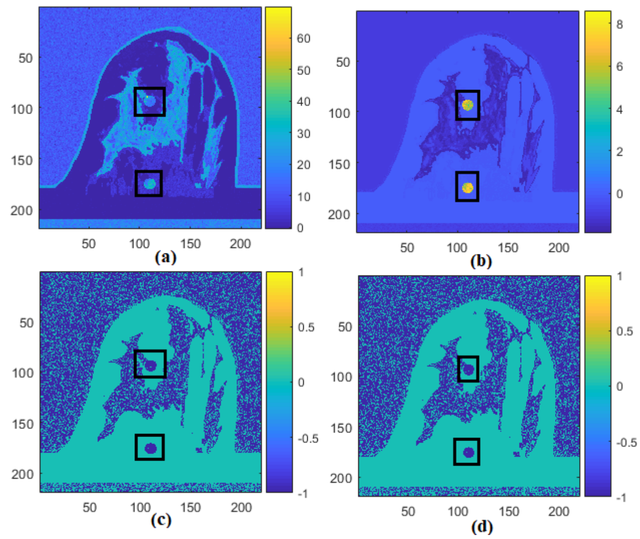

FIGURE 9. Original image of breast 6: (a) real part, (b) imaginary part; Reconstructed image of breast 6: (c) real part, (d) imaginary part.

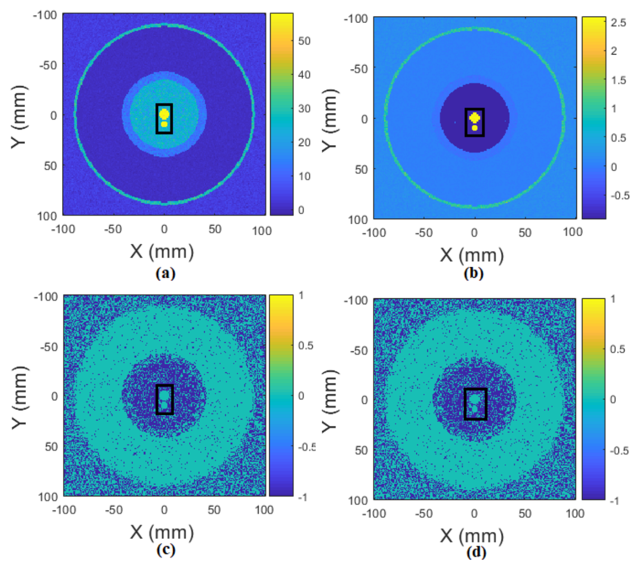

FIGURE 10. Original image of breast 7: (a) real part, (b) imaginary part; Reconstructed image of breast 7: (c) real part, (d) imaginary part.

(imaginary part) when the breast and transceivers immersed in medium ($\varepsilon_r = 12$, $\sigma = 0.4$ S/m). Therefore, the medium of ($\varepsilon_r = 12$, $\sigma = 0.4$ S/m) was assumed as background for the following simulation scenarios.

Figure 6(a) and Figure 6(b) demonstrate the 2D views of the 3D breast 3 ($90 \times 90 \times 50\text{mm}^3$) including skin (3 mm), fat, fibro-glandular 1 (42 mm in radius), fibro-glandular 2 (34 mm in radius), two tumors (3 and 5 mm in radius, squared in black) located at (0 mm, 0 mm, 0 mm) and (0 mm, 10 mm, 0 mm). Figures 6(c) and 6(d) show the reconstructed images of the breast under test over $1 \sim 4$ GHz band. Two tumors could be observed in both real and imaginary parts of the reconstructed images with correct information on their size, shape, and location.

C. MRI-DERIVED BREAST PHANTOMS

Figure 7 shows the original and reconstructed images of breast model 4 over the $1 \sim 4$ GHz frequency band. No tumor embedded inside this MRI-derived breast phantom ($219 \times 219 \times 273$ voxels). A cross-section corresponding to slice number 136 of the breast 4 was selected. Results showed that some internal structures of the breast could be observed in both real and imaginary parts of the reconstructed images with correct information on their size, shape, and location.

Figure 8 displays the original and imaging results of breast 5, including two tumors (5 mm in radius) over the frequency band of $1 \sim 4$GHz. The breast and transceivers immersed in the lossless background ($\varepsilon_r = 12$, $\sigma = 0$ S/m). The internal structures of the breast and two tumors could be clearly observed in both real and imaginary parts of the reconstructed images with correct information on their size, shape and position.

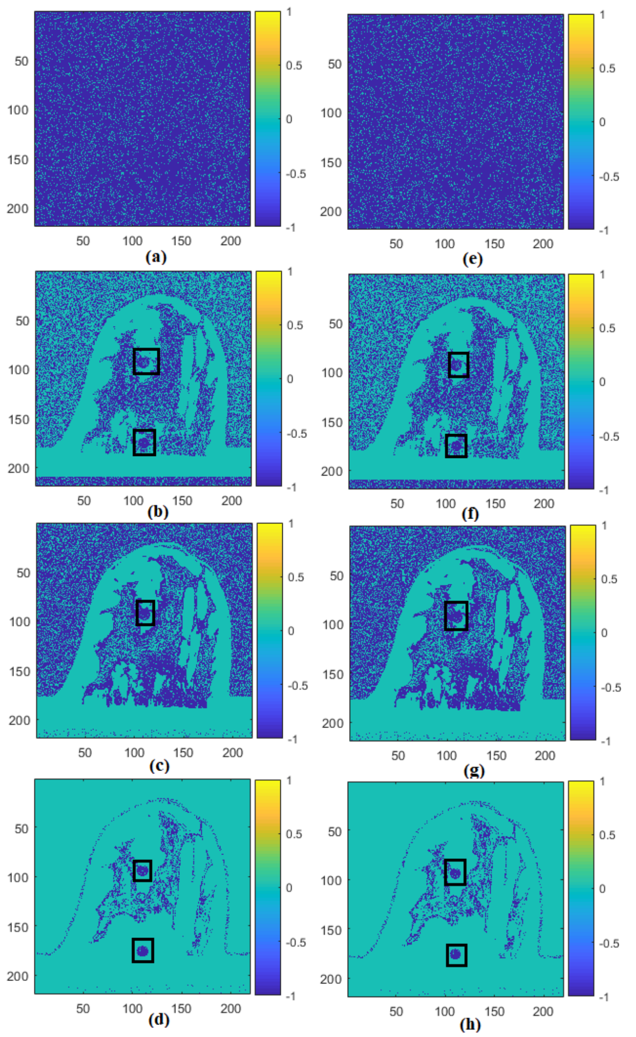

FIGURE 11. Real part of reconstructed image of breast 6 at frequency of: (a) 1 GHz, (b) 2 GHz, (c)3 GHz, (d)4 GHz; Imaginary part of reconstructed image of breast 6 at frequency of: (e) 1 GHz; (f) 2 GHz; (g)3 GHz; (h) 4 GHz.

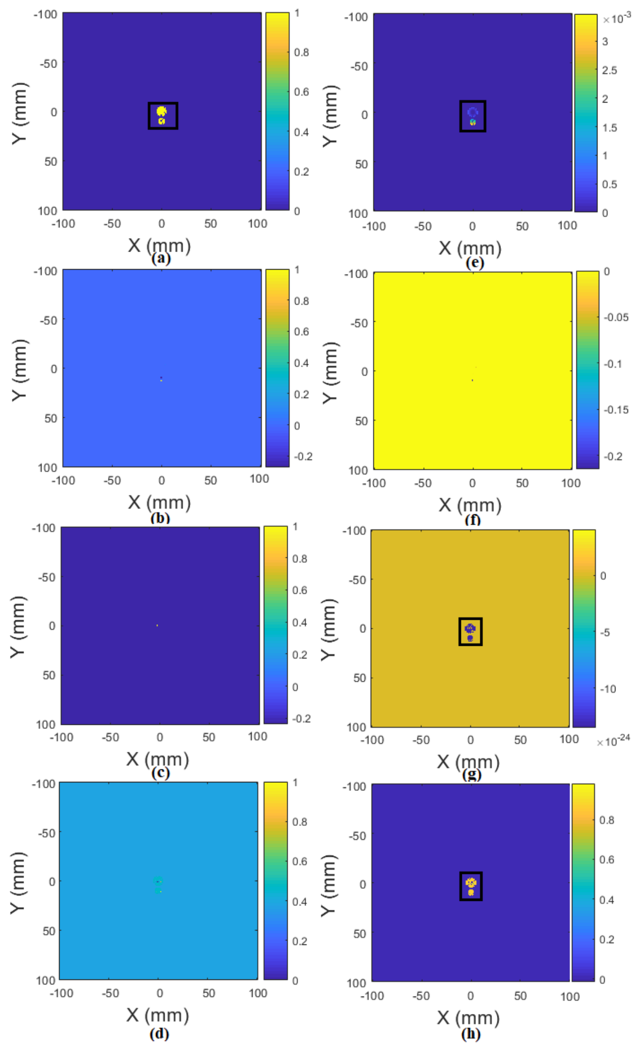

FIGURE 12. Real part of reconstructed image of breast model 7 at frequency of: (a) 1 GHz, (b) 2 GHz, (c)3 GHz, (d) 4 GHz; Imaginary part of reconstructed image of breast model 7 at frequency of: (e) 1 GHz, (f) 2 GHz, (g) 3 GHz, (h) 4 GHz.

D. NOISE BREAST PHANTOMS

We tested the proposed method with noise breast models to evaluate the effectiveness and accuracy of the proposed method. Figure 9 and Figure 10 display the original and multi-frequency HMI results of noise breast 6 and breast 7 at the frequency range of 1GHz to 4GHz, respectively. Each noise breast consisted of 10% Gaussian noise. The breast and transceivers immersed in the lossless medium ($\varepsilon_r = 12$, $\sigma = 0$ S/m). Results suggested that the detailed internal structures of the breast, including tumors, could be successfully represented in the reconstructed images (both real and imaginary parts).

E. COMPARISON STUDY OF SINGLE AND MULTI-FREQUENCY HMI

A comparison study of single and multi-frequency HMI was conducted to investigate the effectiveness, accuracy, and sensitivity of the proposed method.

Figure 11 demonstrates the original and single frequency HMI results of breast 6 at a working frequency of 1 GHz, 2 GHz, 3 GHz, and 4 GHz. The breast and transceivers immersed in the lossless medium ($\varepsilon_r = 12$, $\sigma = 0$ S/m). Results showed that two lesions could be identified in both real and imaginary parts of the reconstructed images at the frequency of 2 GHz and 4 GHz, only one tumor could be observed in the reconstructed image at the working frequency of 3 GHz. The internal structures of the breast and tumors could not be observed in the reconstructed images at the working frequency of 1 GHz.

Figure 12 shows the original and single frequency HMI results of breast 7 at a working frequency of 1 GHz, 2 GHz, 3 GHz, and 4 GHz. The breast and transceivers immersed in the lossless background ($\varepsilon_r = 12$, $\sigma = 0$ S/m). Results suggested that two tumors could be identified in both real and imaginary of the reconstructed images at the working frequency of 1 GHz, they could be detected in the imaginary part of the imaging results at 3 GHz and 4 GHz, no any tumor could be observed in the reconstructed images at 2 GHz.

However, the internal structures of the breast under test could not be identified.

Comparing the imaging results of multi-frequency HMI (Figures 6 and 10) with that of single frequency HMI (Figures 11 and 12), it can be seen that the multi-frequency HMI algorithm could successfully detect small breast lesions with more accurate information on their shape, size, and location than that of single frequency HMI. Moreover, the detailed internal structures of the breasts could be fully detected using multi-frequency imaging approach.

TABLE 2. PSNR of breast model 7 using different frequencies.

Frequency (GHz)	1	2	3	4	1~4
PSNR (dB)	14.5803	14.5608	14.5598	14.5671	14.8796
MSE	0.0325	0.0350	0.0350	0.0300	0.0325

Table 2 demonstrates the performances of single and multi-frequency HMI for imaging of breast 7 at different working frequencies. Compared to single frequency HMI, the multi-frequency HMI approach produces better image performance at the frequency of $1 \sim 4$ GHz. The results agreed with the imaging results, as demonstrated in Figures 10 and 12.

Color bars in breast models present the dielectric profile of the breasts, while they in reconstructed images demonstrate the scattered energy distributions.

V. CONCLUSION

This paper presented the modeling of multi-frequency HMI algorithm for detecting breast lesions. A realistic computer system was developed to demonstrate the working principle of the proposed multi-frequency HMI. Various numerical evaluations were performed to investigate the effectiveness, sensitivity, and accuracy of the proposed method for breast lesion detection under practical consideration. Both noise free and noise breast models were studied in this premilitary study, and image resolution was degraded in noise breasts. Additionally, a comparison study of single and multi-frequency HMI was carried out to investigate the effectiveness and accuracy of the proposed method for breast lesion detection.

The results demonstrated that the multi-frequency HMI could fully reconstruct the internal structures of the breast under test and identify small tumors with more accurate results on their size, shape, and location. The tumors could be successfully identified in the breast images even when they embedded in dense tissue such as the fibro-glandular. The proposed method can improve image resolution, which has the potential to develop a helpful vision tool for investigating microwave diagnostic techniques.

Future work will focus on practical evaluations of the proposed method, including the design and development of a clinically applicable prototype as well as the experimental validations of the technique on more realistic scenarios.

REFERENCES

[1] M. R. Mohebian, H. R. Marateb, M. Mansourian, M. A. Mañanas, and F. Mokarian, "A hybrid computer-aided-diagnosis system for prediction of breast cancer recurrence (HPBCR) using optimized ensemble learning," *Comput. Struct. Biotechnol. J.*, vol. 15, pp. 75–85, Dec. 2017.

[2] A. Migowski, "Early detection of breast cancer and the interpretation of results of survival studies," *Ciencia Saude Coletiva*, vol. 20, no. 4, p. 1309, Apr. 2015.

[3] K.-J. Joo, J.-W. Shin, K.-R. Dong, C.-S. Lim, W.-K. Chung, and Y.-J. Kim, "A study on the dependence of exposure dose reduction and image evaluation on the distance from the dental periapical X-ray machine," *J. Korean Phys. Soc.*, vol. 63, no. 9, pp. 1824–1831, 2013.

[4] T. Onega, L. E. Goldman, R. L. Walker, D. L. Miglioretti, D. S. Buist, S. Taplin, B. M. Geller, D. A. Hill, and R. Smith-Bindman, "Facility mammography volume in relation to breast cancer screening outcomes," *J. Med. Screening*, vol. 23, no. 1, pp. 31–37, Mar. 2016.

[5] A. M. Hassan and M. El-Shenawee, "Review of electromagnetic techniques for breast cancer detection," *IEEE Rev. Biomed. Eng.*, vol. 4, pp. 103–118, 2011.

[6] B. N. Hellquist, K. Czene, A. Hjälm, L. Nyström, and H. Jonsson, "Effectiveness of population-based service screening with mammography for women ages 40 to 49 years with a high or low risk of breast cancer: Socioeconomic status, parity, and age at birth of first child," *Cancer*, vol. 118, no. 2, pp. 1170–1171, Jan. 2012.

[7] D. O'Loughlin, M. O'Halloran, B. M. Moloney, M. Glavin, E. Jones, and M. A. Elahi, "Microwave breast imaging: Clinical advances and remaining challenges," *IEEE Trans. Biomed. Eng.*, vol. 65, no. 11, pp. 2580–2590, Nov. 2018.

[8] N. Z. Naghsh, A. Ghorbani, and H. Amindavar, "Compressive sensing for microwave breast cancer imaging," *IET Signal Process.*, vol. 12, no. 2, pp. 242–246, Apr. 2018.

[9] D. W. Winters, J. D. Shea, P. Kosmas, B. D. Van Veen, and S. C. Hagness, "Three-dimensional microwave breast imaging: Dispersive dielectric properties estimation using patient-specific basis functions," *IEEE Trans. Med. Imag.*, vol. 28, no. 7, pp. 969–981, Jul. 2009.

[10] M. Klemm, J. A. Leendertz, D. Gibbins, I. J. Craddock, A. Preece, and R. Benjamin, "Microwave radar-based differential breast cancer imaging: Imaging in homogeneous breast phantoms and low contrast scenarios," *IEEE Trans. Antennas Propag.*, vol. 58, no. 7, pp. 2337–2344, Jul. 2010.

[11] M. Klemm, I. Craddock, J. Leendertz, A. Preece, and R. Benjamin, "Experimental and clinical results of breast cancer detection using UWB microwave radar," in *Proc. IEEE Antennas Propag. Soc. Int. Symp.*, San Diego, CA, USA, Jul. 2008, pp. 1–4.

[12] N. K. Nikolova, "Microwave imaging for breast cancer," *IEEE Microw. Mag.*, vol. 12, no. 7, pp. 78–94, Dec. 2011.

[13] S.-H. Son, N. Simonov, H.-J. Kim, J.-M. Lee, and S.-I. Jeon, "Preclinical prototype development of a microwave tomography system for breast cancer detection," *Etri J.*, vol. 32, no. 6, pp. 901–910, Dec. 2010.

[14] K. C. Kwon, Y. T. Lim, C. H. Kim, N. Kim, C. Park, K. H. Yoo, S. H. Son, and S. I. Jeon, "Microwave tomography analysis system for breast tumor detection," *J. Med. Syst.*, vol. 36, no. 3, pp. 1757–1767, Jun. 2012.

[15] X. Zhu, Z. Zhao, J. Wang, J. Song, and Q. H. Liu, "Microwave-induced thermal acoustic tomography for breast tumor based on compressive sensing," *IEEE Trans. Biomed. Eng.*, vol. 60, no. 5, pp. 1298–1307, May 2013.

[16] P. M. Meaney, A. H. Golnabi, N. R. Epstein, S. D. Geimer, M. W. Fanning, J. B. Weaver, and K. D. Paulsen, "Integration of microwave tomography with magnetic resonance for improved breast imaging," *Med. Phys.*, vol. 40, no. 10, Oct. 2013, Art. no. 103101.

[17] N. R. Epstein, P. M. Meaney, and K. D. Paulsen, "3D parallel-detection microwave tomography for clinical breast imaging," *Rev. Sci. Instrum.*, vol. 85, no. 12, Dec. 2014, Art. no. 124704.

[18] P. M. Meaney, M. W. Fanning, R. M. di Florio-Alexander, P. A. Kaufman, S. D. Geimer, T. Zhou, and K. D. Paulsen, "Microwave tomography in the context of complex breast cancer imaging," in *Proc. Annu. Int. Conf. IEEE Eng. Med. Biol.*, Aug./Sep. 2010, pp. 3398–3401.

[19] M. A. Elahi, D. O'Loughlin, B. R. Lavoie, M. Glavin, E. C. Fear, and M. O'Halloran, "Evaluation of image reconstruction algorithms for confocal microwave imaging: Application to patient data," *Sensors*, vol. 18, no. 6, p. 1678, May 2018.

[20] J. M. Sill and E. C. Fear, "Tissue sensing adaptive radar for breast cancer detection—Experimental investigation of simple tumor models," *IEEE Trans. Microw. Theory Techn.*, vol. 53, no. 11, pp. 3312–3319, Nov. 2005.

[21] S. K. Davis, E. J. Bond, S. C. Hagness, and B. D. Van Veen, "Microwave imaging via space-time beamforming for early detection of breast cancer: Beamformer design in the frequency domain," *J. Electromagn. Waves Appl.*, vol. 17, no. 2, pp. 357–381, 2003.

[22] M. Elsdon, D. Smith, M. Leach, and S. J. Foti, "Experimental investigation of breast tumor imaging using indirect microwave holography," *Microw. Opt. Technol. Lett.*, vol. 48, no. 3, pp. 480–482, Mar. 2010.

[23] L. Wang and M. Fatemi, "Compressive sensing holographic microwave random array imaging of dielectric inclusion," *IEEE Access*, vol. 6, pp. 56477–56487, 2018.

[24] L. Wang, A. M. Al-Jumaily, and R. Simpkin, "Investigation of antenna array configurations using far-field holographic microwave imaging technique," *Progr. Electromagn. Res. M*, vol. 42, pp. 1–11, Jun. 2015.

[25] M. G. Garcia, L. J. Roca, S. C. Cascante, S. B. Boris, and J. R. Robert, "3D UWB magnitude-combined tomographic imaging for biomedical applications. Algorithm validation," *Radioengineering*, vol. 20, no. 2, pp. 366–372, Jun. 2011.

[26] S. Silver, *Microwave Antenna Theory and Design*. London, U.K.: S. Peter Peregrinus Ltd., 1984.

[27] R. Levanda and A. Leshem, "Synthetic aperture radio telescopes," *IEEE Signal Process. Mag.*, vol. 27, no. 1, pp. 14–29, Dec. 2009.

[28] L. Wang, A. M. Al-Jumaily, and R. Simpkin, "Imaging of 3-D dielectric objects using far-field holographic microwave imaging technique," *Prog. Electromagn. Res. B*, vol. 61, pp. 135–147, Oct. 2014.

[29] X. Qu, X. Cao, D. Guo, C. Hu, and Z. Chen, "Combined sparsifying transforms for compressed sensing MRI," *Electron. Lett.*, vol. 46, no. 2, pp. 121–123, Jan. 2010.

[30] L. Wang, A. M. Al-Jumaily, and R. Simpkin, "Holographic microwave imaging for medical applications," *J. Biomed. Sci. Eng.*, vol. 6, no. 8, pp. 823–833, Jul. 2013.

[31] L. Wang, *Basic Principles and Potential Applications of Holographic Microwave Imaging*. New York, NY, USA: ASME Press, 2016.

[32] M. Guardiola, S. Capdevila, J. Romeu, and L. Jofre, "3-D microwave magnitude combined tomography for breast cancer detection using realistic breast models," *IEEE Antennas Wireless Propag. Lett.*, vol. 11, pp. 1622–1625, 2013.

[33] Italian National Research Council. *An Internet Resource for the Calculation of the Dielectric Properties of Body Tissues in the Frequency Range 10 Hz—100 GHz*. Accessed: May 16, 2019. [Online]. Available: http://niremf.ifac.cnr.it/tissprop/

[34] E. Zastrow, S. K. Davis, M. Lazebnik, F. Kelcz, B. D. Van Veem, and S. C. Hagness. *Database of 3D Grid-Based Numerical Breast Phantoms for use in Computational Electromagnetics Simulations*. Accessed: May 16, 2019. [Online]. Available: http://uwcem.ece.wisc.edu/MRIdatabase/

LULU WANG (M'12) received the M.E. (Hons.) and Ph.D. degrees from the Auckland University of Technology, New Zealand, in 2009 and 2013, respectively, where she was a Research Fellow with the Institute of Biomedical Technologies, from 2013 to 2015. In 2015, she became an Associate Professor of biomedical engineering with the Hefei University of Technology. In 2019, she became a Full Professor of biomedical engineering with the College of Health Science and Environmental Engineering, Shenzhen Technology University. She is the first author of over 60 peer-reviewed publications, two ASME books, five book chapters, and four issued patents. Her research interests include electromagnetic theory and imaging applications, medical devices, and computational mechanics. She is also a member of ASME, AAAS, PSNZ, and IPENZ. She received the Multiple National and International Awards from various professional societies and organizations.